



Microbursts of the UV atmospheric emission in the auroral zone

P.A. Klimov^{a,*}, V.D. Nikolaeva^a, R.E. Saraev^{a,b}, K.D. Shchelkanov^{a,b}, A.A. Belov^{a,b},
B.V. Kozelov^c, A.S. Murashov^a, A.V. Roldugin^c, S.A. Sharakin^a

^a Skobeltsyn Institute of Nuclear Physics, Lomonosov Moscow State University, 119234 Moscow, Russia

^b Faculty of Physics, Lomonosov Moscow State University, 119234 Moscow, Russia

^c Polar Geophysical Institute, 15, Khalturina St, 183010 Murmansk, Russia

Received 21 February 2024; received in revised form 20 June 2024; accepted 23 June 2024

Abstract

In this paper we present data on the UV-microburst (300–400 nm flashes with a duration less than 1 s) measurements in the auroral zone. Measurements were performed during the period 09.2021–04.2022 by the highly sensitive imaging photometer installed at the Verkhnetulomsky observatory of the Polar Geophysical Institute. It is shown that microbursts are grouped in a series with a duration from 10 s to 10 min. They were observed in relatively quiet geomagnetic conditions ($K_p < 3$) at the southern boundary of the auroral oval in the evening magnetic local time (MLT) sector. UV-microbursts are observed in different observational conditions (clouds, transparent clouds and clear sky) and spatially represent various patterns: uniform diffuse illumination, local spots. Joint analyses of the optical measurements and satellite data on charged particle fluxes demonstrates that an auroral oval, characterized by a plasma, is placed to the north of the observatory. At the same time increased flux of electrons with energy more than 100 keV is observed at the same L-shell and MLT sector. The possible origin of the UV-microbursts is a precipitation of energetic electrons from a poleward boundary of the outer radiation belt in a form of relativistic electron microbursts is discussed.

© 2024 COSPAR. Published by Elsevier B.V. All rights are reserved, including those for text and data mining, AI training, and similar technologies.

Keywords: UV-microbursts; Fast imaging photometer; Aurora; Relativistic electron microbursts

1. Introduction

Study of the optical and near ultraviolet (UV, 300–400 nm) emission of the atmosphere is an efficient instrument for researching various physical phenomena which deposit their energy in the atmosphere. For example, measurements of extensive air showers fluorescent and Cherenkov radiation in a sub millisecond temporal range is a well known and widely used technique for extragalactic ultra-high-energy cosmic rays studies (Abraham et al., 2010; Tokuno et al., 2011; Klimov et al., 2017). Satellite measure-

ments of transient near-UV emission above thunderstorm regions provide important information on the spatial and temporal structure of so-called Transient luminous events (TLEs) (Marshall et al., 2015; Klimov et al., 2019, Casolino et al., 2023).

In the auroral zone the fastest objects are pulsating aurora (PsA) and flickering aurora which have a complicated temporal structure which reflect their origin mechanism in the magnetosphere. The typical period of luminosity pulsations ranges from several to several tens of seconds. These are the main pulsations, developing according to the on/off pattern. The duration of the on phase lies, as a rule, within two typical ranges: 0.2–0.5 s and 2–6 s (Nishimura et al., 2020). The characteristic height of the

* Corresponding author.

E-mail address: pavel.klimov@gmail.com (P.A. Klimov).

<https://doi.org/10.1016/j.asr.2024.06.060>

0273-1177/© 2024 COSPAR. Published by Elsevier B.V. All rights are reserved, including those for text and data mining, AI training, and similar technologies.

pulsating glow corresponds to the lower E-layer of the atmosphere and is about 90–110 km (Kataoka et al., 2016), which indicates that auroral pulsations are generated by the precipitation of electrons with an energy of 10–40 keV (Turunen et al., 2009). On the other hand, it was demonstrated by Miyoshi et al. (2020) that both PsA and microbursts of relativistic electrons are products of the interaction of chorus waves with particles, i.e. microbursts of relativistic and subrelativistic electrons are the high-energy (>100 keV) tail of pulsating auroral electrons. These electrons fall significantly deeper into the atmosphere and increase the level of ionization to 70 km. Thus PsA are related to electron precipitation in a wide energy range.

Mechanisms of formation and losses in radiation belts are one of the most important questions of magnetospheric physics, especially in a subsecond temporal scale. And this question can be addressed by using the optical methods and we demonstrate it in the current work.

Since radiation belts discovery it has been shown in a number of studies that wave-particle interaction is a main driver for outer radiation belt (ORB) dynamics, particle acceleration and loss in general in the long time scales (Claudepierre et al., 2020). For a subsecond process there is still an open questions: what type of magnetospheric plasma waves lead to electron precipitations in the form of microbursts.

Microbursts of electrons are intense pulses of electron precipitation that typically last ≈ 100 ms (Shumko et al., 2021). First indication and indirect measurements of microbursts were done by balloon-borne registration of bremsstrahlung X-rays in auroral zone (Anderson, & Milton, 1964). Microbursts usually appear as a train of pulses. Simultaneous conjugate electron microburst group precipitation were measured as groups of bremsstrahlung X-ray microbursts ($E > 25$ keV) during a substorm recovery phase by a balloon-borne scintillation counter over Roberval, Quebec, Canada (Siren et al., 1980).

Microburst energies span from tens of keV up to > 1 MeV. The microburst L-shell and magnetic local time (MLT) distributions peaks in the outer radiation belt L-shells (99 % of bursts occur between $L = 3$ and $L = 8$) and in the 0–12 MLT region (Lorentzen et al., 2001; O'Brien et al., 2003). Measurements of relativistic electron microbursts (REMs) are important to understand how REMs contribute to the global flux decay of the outer belt during storms and do they correlate with loss of outer belt electrons? Greeley et al. (2019) demonstrate that the microburst contribution to global loss coupling is predominant in the quasi-trapped population of radiation belt electrons while having negligible influence on the untrapped and stably trapped populations.

Substorm-driven Pc4–5 ultra low frequency (ULF) pulsations modulate chorus waves, and thus provide the driver for pulsating particle precipitation into the Earth's atmosphere (Jaynes et al., 2015). A few-Hz modulation of individual chorus elements that coincides with the same

modulation in a nearby pulsating aurora patch was observed. Later a correlation of patchy aurora and REM measured by SAMPEX was found. On the other hand, electromagnetic ion cyclotron (EMIC) waves can lead to REMs (Shumko et al., 2022), for more details, see discussion at the end of the paper.

The role of high energy charged particles in the PsA formation is an important aspect of their studies. Measurements conducted using incoherent scatter radars (Miyoshi et al., 2015, Tesema et al., 2020) indicate the presence of a significant population of electrons with energies above 50 keV. These high-energy electrons contribute to additional ionization and luminosity at altitudes ranging from 60 to 80 km.

In this paper we present a statistical study of UV-microbursts measured by a fast imaging photometer at Verkhnetulomsky observatory (68° 35' 29.61" N, 31° 45' 19.18" E, Kola peninsula) and discuss their possible magnetospheric origin in the context of relativistic electron microbursts.

2. Instruments

The UV-microbursts discussed in this paper were measured at Verkhnetulomsky observatory (VTL) by a recently developed and installed imaging photometer. The photometer consists of two main parts: lens telescope and the spectrometer. Both use photomultiplier tubes as a photo sensor which allows it to achieve very high sensitivity. Multi-anode PMTs of telescope operate in a single photon-counting mode. The lens diameter is 5 cm (geometrical area of entrance pupil is near 20 cm²). Spectrometer is a matrix of single-anode PMTs with interference filters in front of photocathodes. Two channels are of great interest: 391 nm and 337 nm – fast emissions of molecular nitrogen bands. In detail the detector is described by Belov et al. (2022). This photometer is a first one of the Pulsating Aurora Imaging System (PAIPS) deployed in the Kola peninsula (Klimov et al., 2022b) and aimed to provide stereo measurements of spatial PsA structures with high temporal resolution.

Microbursts were selected from the VTL photometer as follows. At the first stage, an automatic trigger algorithm was applied to search for short peaks throughout the entire database. Then, by visual inspection of light curves and all-sky camera (ASC) images, all artifacts, quasi-periodic pulsations, anthropogenic flashes, and pulsating auroras were excluded since they have typical spatio-temporal structure as was described by Klimov et al. (2022b). Events associated with meteor, satellite, and aircraft flybys were then excluded from the database. These events were detected visually by characteristic spatiotemporal patterns. When registering a meteor, a short gaussian-shaped peak with a characteristic spatial structure on the photodetector matrix in the form of a narrow track is observed. The satellite flies across the entire field of view (FOV), leaving a track with a quasi-constant glow intensity. When an aircraft enters the

FOV, it is characterized by the presence of equidistant short peaks in the light curve associated with the blinking of the side lights.

In addition to photometers we use regular all-sky cameras (ASC) which are installed at the same optical box with the photometer (Kozelov et al., 2011). These cameras demonstrate meteorological conditions of measurements: presence of clouds, their movement, other sources (moon, stars). Camera images allow us to recognize the presence of polar lights and their variability.

For the additional analyses of the magnetospheric conditions, aurora oval position and charged particles fluxes a number of satellite instruments were used. To demonstrate the position of microbursts in relation to the oval we have used DMSP plasma detectors data. The Defense Meteorological Satellites Program (DMSP) was introduced in the mid-sixties (Hall, 2001). Each DMSP satellite has a sun-synchronous orbit at an altitude of approximately 830 km above the Earth's surface. The orbital time is 101 min. SSJ detectors onboard DMSP measure precipitating particle fluxes in 19 different channels from 30 eV to 30 keV. Particles of these energies penetrate to ionospheric altitudes up to 80 km and serve as the main source of ionization at night and make a significant contribution to the ionization of the auroral ionosphere during the daytime. DMSP satellites data on particle precipitation are publicly available with 1 s temporal resolution at [<https://www.ncei.noaa.gov/data/dmsp-space-weather-sensors/>] (Redmon et al., 2017).

To compare with high energy electrons (>100 keV) we have used METEOR-M2 detectors measurements. The satellite METEOR-M2 has a polar sun-synchronous circular orbit with an inclination of 98.8° and an altitude of 825 km. Charged particle detectors on board the METEOR-M2 include a horizontal spectrometer MSGI-M (DAS4, 90°) and the vertical spectrometer SKL-M (DAS4, 0°). These detectors measure electron fluxes with energies in the range of 100 keV–8 MeV. Vertical spectrometer is directed approximately along the magnetic field at high latitudes, and it measures mainly precipitating charged particles while the horizontal one – trapped particles. The MSGI-M also contains an electrostatic analyzer measuring electron flux in the energy range from 0.032 keV to 16.64 keV. More details can be found, for example, in Kugusheva et al. (2021).

3. Results

3.1. UV-microbursts phenomenology

Data of the season 2021/2022 were analyzed. In total the detector obtained 163 nights (~2085 h) of measurements between September 29, 2021 to April 19, 2022. Measurements were conducted in various conditions in a monitoring mode with temporal resolution of 41 ms. In total 36 events of microbursts were found and analyzed. Each event represents a group of pulse series. The series is a number of

subsequent pulses of UV emission which illuminate the whole photodetector. Thus, their angular size exceeds the detector FOV of 9 degrees.

Maximum duration of the event is 2 h. The duration of series which comprise the event varies in a range from 20 s to ~1 min and consists of a number of separate pulses. Each pulse usually has a complicated structure with a single time sample high intensity peak and a subsequent prolonged afterglow. Time interval between pulses is not constant and varies in a range between 100 ms and 5 s. Two examples of different events are shown in Fig. 1. On the left panel a long group of series is presented. On the right panel – a short single series.

On the left part of Fig. 1 it is well seen that a long series of bursts (from 15:38 to 15:50, i.e. 12 min) occurs simultaneously with slow UV emission variations caused by clouds. Sharp steps in the emission, intensity are caused by switching on and off lights near the observatory. One of this average emission intensity sudden change is shown in the insert panel of the left figure. Analyses of the all-sky camera image showed that at that moment the street lamp in the observatory was turned off. Microbursts exist when anthropogenic lights are switched on and switched off. This proves that they are definitely not man-made light pulses. The distributions by peak amplitude and duration are shown in Fig. 2. The duration (full width at half maximum, FWHM) of most of the pulses is less than 100 ms, the typical amplitude is around 500–1000 counts which approximately corresponds to the intensity of the emission on the entrance window of 10^4 – 10^5 photon/cm² sr s.

The complete list of measures series of microbursts is presented in Appendix A. It can be seen that most of the events are measured during cloudy conditions, but with visible stars that means that these clouds are moving and semi-transparent.

For all series of UV-microbursts data of an all-sky camera was analyzed. For one event there is a corresponding rise of intensity during 38 s and complicated temporal structure in ASC data which resembles a peak sequence (Fig. 3). The amplitudes of the signals in the camera and photometer also correspond to each other: at the beginning and at the end of the series they are maximum. The intensity of these UV-microbursts is maximum among all 36 cases and only this one is seen in camera. For other events, sensitivity of an all-sky camera is not enough to measure such events. Unfortunately dense cloud coverage and significant scattering does not allow us to understand the position of the UV emission source.

3.2. Position of UV-microbursts relative to the auroral oval: Comparison with satellite charge particles detectors measurements and empirical model

For each event direct measurements of the charged particles flux, conducted on board the satellites located at the same MLT sector and L-shell were studied. We have used data from two satellites: DMSP and METEOR-M2.

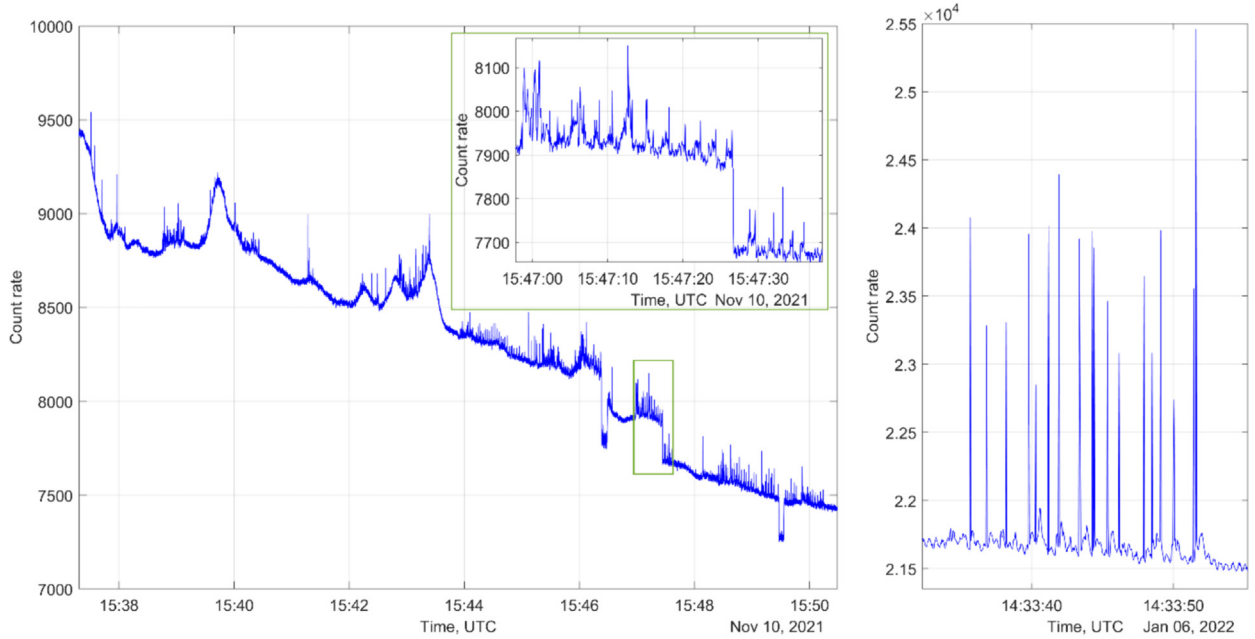


Fig. 1. Left: example of a long series. The insert panel demonstrates the moment of street light switching off. Right: A short series of microbursts.

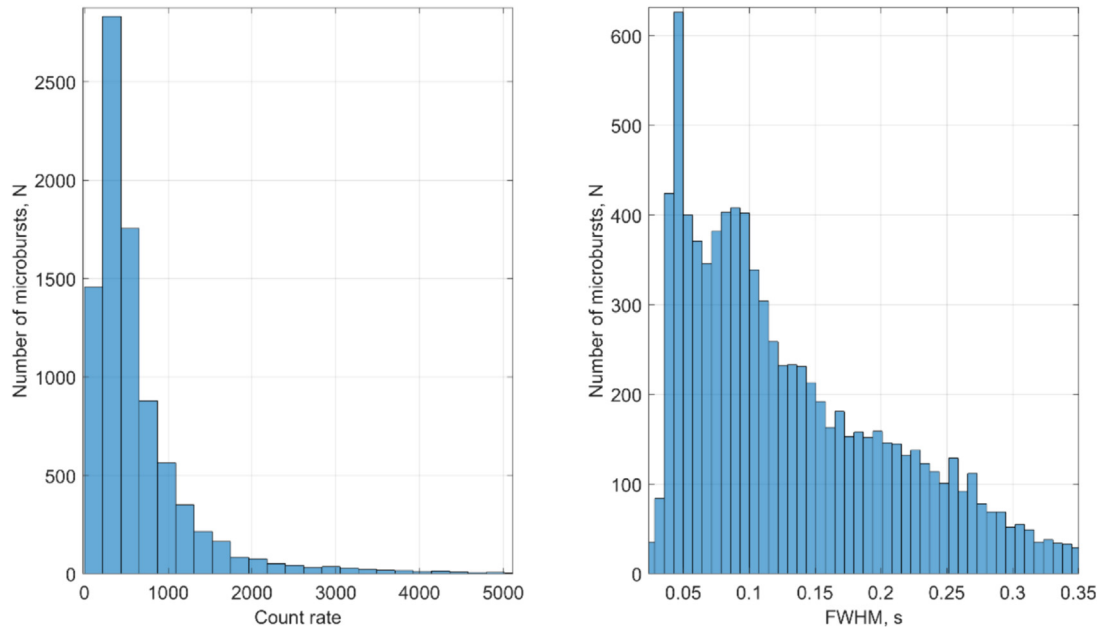


Fig. 2. The distributions of UV-microbursts on peak amplitude (left panel) and duration (right panel).

First of all the position of satellites were analyzed to find coincidences of observational area. And only 6 coincidences were found which are described below.

For three events (December, 16 and two events measured on December, 22) a DMSP was close to the VTL. The results are shown in Fig. 4. Vertical red line corresponds to $L = L_{VTL} = 6$. The VTL observatory is located significantly further south than the aurora oval. The satellite flew from south to north, the distance between VTL and the location of the satellite where the charged particle

flux increasing was measured is around 500 km. This result is expected since the geomagnetic activity is low. The DMSP satellite has no high energy electrons detectors thus to understand the possible relation of UV-microbursts to more energetic components we have used METEOR-M2 satellite data.

Three examples of METEOR-M2 measurements are shown on Fig. 5. Blue lines demonstrate the high energy electrons fluxes: >100 keV (solid line) and >300 keV (dashed line), red line – low energy plasma flux

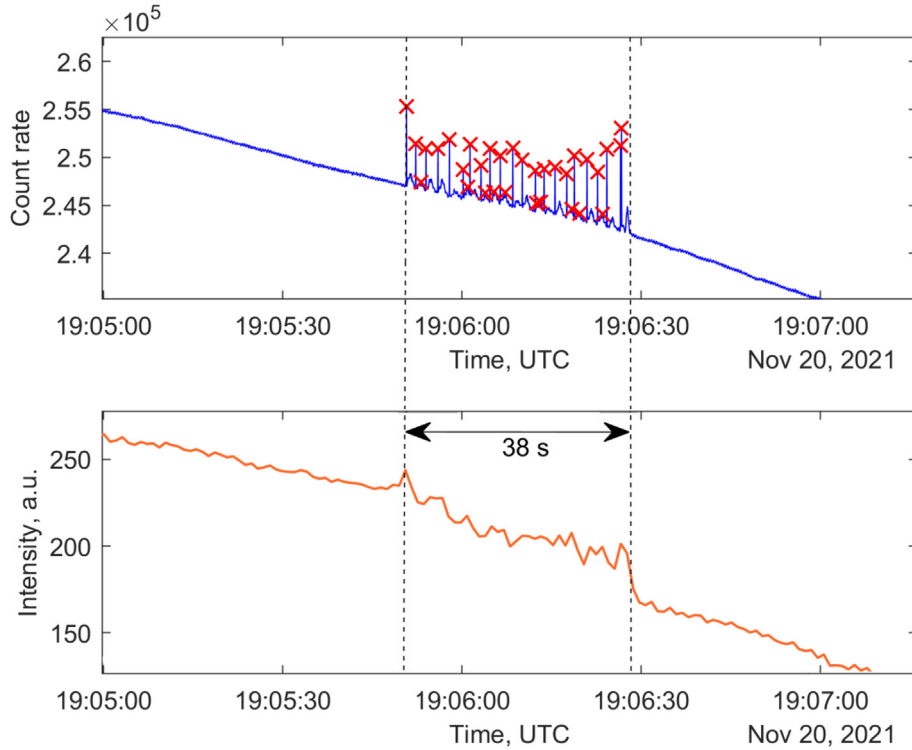


Fig. 3. Simultaneous measurements of photometer and ASC conducted on 20.11.2021. Upper plot – lightcurve measured by photometer, bottom plot – ASC 49 central pixels integral lightcurve.

(0.032–16.64 keV). Data from a vertically located detector (DAS4_vrt) were used. At high latitudes it measures the flux along the magnetic field line, which means precipitating electrons. The time corresponds to UV-microbursts measurements; the longitude of satellite trajectory is close to VTL (MLT difference is 0.37 h, 1.92 h and 0.91 h for November 10, December 16 and December 22 respectively). It can be seen that above VTL ($L_{VTL} = 6$) the increase of energetic electrons flux is observed, while low energy electrons are precipitating significantly higher in latitude.

Thus, for these events we can conclude that they are observed simultaneously with increased energetic electron fluxes (more than 100 keV), measured by METEOR-M2 satellite and south of the auroral oval (low energy plasma flux, measured by DMSP and METEOR-M2).

Due to the lack of direct measurements for all events, their position relative to the auroral oval was studied statistically. The statistical auroral precipitation characteristics were obtained using the OVATION-Prime model (Newell et al., 2009; Newell et al., 2010). The OVATION-Prime model provides the spatial distribution of electron precipitation parameters at high latitudes ($CGMLat = 50^\circ\text{--}90^\circ$) on a discrete grid ($MLT \times CGMLat = 0.25 \text{ h} \times 0.25^\circ$) for the moderate geomagnetic conditions ($K_p < 6$). The model is based on the DMSP particle data for two solar cycles and normalized on the OMNI solar wind (SW) parameters in the following form (Newell et al., 2007) $N = v^{4/3} B_T^{2/3} \sin^{8/3}(\theta/2)$, where v is the SW speed; B_T is

the interplanetary magnetic field (IMF) tangential component, $B_T = (B_Z^2 + B_Y^2)^{1/2}$; θ is the IMF clock angle, $\theta = \arctan(B_Y/B_Z)$.

The selected microbursts events were observed during calm geomagnetic conditions. Average IMF and SW parameters for all 36 events, used for the model simulation are: $|B_Y| = 2.33 \text{ nT}$; $|B_Z| = 1.78 \text{ nT}$; $v = 440.3 \text{ km/s}$. Fig. 6 demonstrates microbursts position relative to the statistical distribution of the diffuse and monoenergetic electron precipitation in the auroral zone (Newell et al., 2009) obtained by the OVATION-Prime model.

It is well seen from Fig. 6 that all events are located at the equatorial border of the oval, south of the precipitation zone, which corresponds to average geomagnetic conditions during UV-microbursts observations. Ovation-Prime model takes into account low energy electrons precipitation (below 30 keV). Events are located outside the oval caused by these particles but in the place where high-energy electrons precipitate, which can be seen from measurements of the METEOR-M2 satellite, shown in Fig. 5.

4. Discussion

UV-microbursts were measured in various meteorological conditions by the PAIPS photometer at VTL. For each event a cloud coverage was studied and observation conditions were divided into three categories: clear sky, transparent clouds and clouds. For the second one there are thin

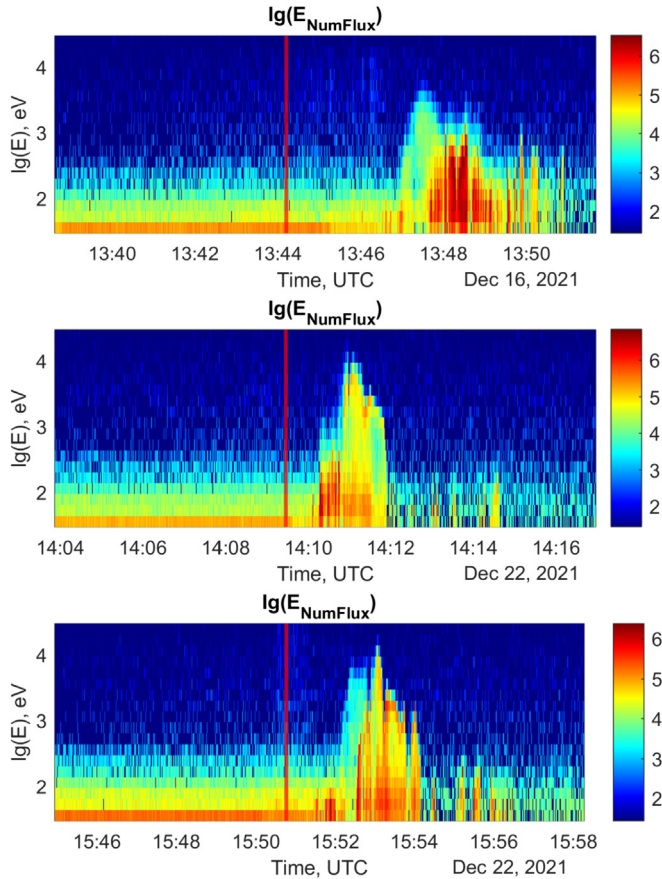


Fig. 4. DMS charge particle flux measurements in the energy range from 30 eV to 30 keV during 3 flights near VTL observatory during UV-microbursts series. Vertical red line corresponds to the crossing the VTL L-shell ($L_{VTL} = 6$).

and transparent clouds in the ASC FOV (stars are well seen), for the third one the sky is totally closed by dense and opaque clouds in the visible range clouds. Observation conditions are given in column 6 of Table A1 of Appendix A. In the majority of cases the sky is cloudy, but for a couple of events the sky is clear. Thus we can compare the temporal structure of events in different conditions.

In Fig. 7 examples of all three cases are shown. The upper panel contains photometer light curves (average signal over the FOV), the middle panel – ASC images, the bottom one – pixel map of a photometer for one peak of each event (the corresponding peak is marked by a vertical red line at the lightcurve below).

The first event was measured on 20.11.2021 and the whole FOV was covered by dense clouds. It is well seen on the ASC image. On the pixel map of the photometer for each microburst there is a corresponding signal in each channel with a higher amplitude in two upper MAPMTs. Optical emission is diffusely scattered in the cloud, the source is located in the area of the upper MAPMTs (north-west relative to VTL).

For the second event (21.11.2021) there are only rare and transparent clouds and mostly not in the photometers FOV (zenith direction which corresponds to the center of

ASC image. The large spot on the ASC image is the Moon, outside the field of view of the photometer. In this case it is possible to see the spatial structure of the source. For the 6th burst one can see two separate spots in the pixel map. The larger spot is seen partially since it is located at the edge of the photometer FOV, while the smaller one is placed in one MAPMT, its angular size is about 4° which corresponds to the lateral dimension ~ 10 km at the altitude of 100 km.

For the third one (07.01.2022) the central part of ASC is totally free of clouds, but the pixel map does not show any local sources in the photometer FOV. All pixels are illuminated quite unevenly, but no obvious spatial structure is observed.

One would expect that the light curves would differ significantly if the sources of these events are different (in the first case they may be associated with clouds, in the second and third are not). But as one can see from the pictures, they are rather similar. Thus, the source is clearly not directly related to the presence of the cloud, and scattering does not affect the temporal structure. At the same time, the appearance of this temporal structure draws attention: individual flashes are sharp peaks, lasting on the order of one time sample (~ 41 ms), followed by a less bright, but long-lasting afterglow.

We have excluded all possible instrumental, anthropogenic or low atmospheric sources of the UV-microbursts and thus consider a possible magnetospheric origin. The most likely candidates for the sources of this transient flare emissions are the so-called relativistic electron microbursts, described in the Introduction.

The first possible indication of their relationship lies in the temporal structure of events. As was described above the single UV-microburst is a short bright peak with a typical duration of one – several time samples (40–150 ms). The same feature we can find in studies of REMs: A typical relativistic microburst has a 100 ms duration (77 % of REMs measured by SAMPEX), and the interquartile range of the duration distribution is 70–140 ms (Shumko et al., 2021).

In (Blake et al., 1996) it was shown that over one satellite pass through the radiation belts it is possible to get multiple relativistic microburst triggers. And based on observations by Douma (2018) REMs are divided into isolated microbursts clusters, which contain only a single relativistic microburst detection (28.8 % of the total microburst cluster dataset), Average Sized Microburst Clusters, which contain 3 individual microburst (9.5 % of the total microburst cluster dataset), and substantial microburst cluster – microburst clusters composed of 50 individual microburst detections. Substantial microburst cluster is only 20 events in the total database gathered during 10 years of SAMPEX operation from 1997 to 2006.

In our case all 36 events represent series or groups of series and are consistent with SAMPEX REM clusters observations. Single UV-microbursts are also seen but are not considered in this paper since we can't reliably eliminate the instrument effect for an individual single-pulse event.

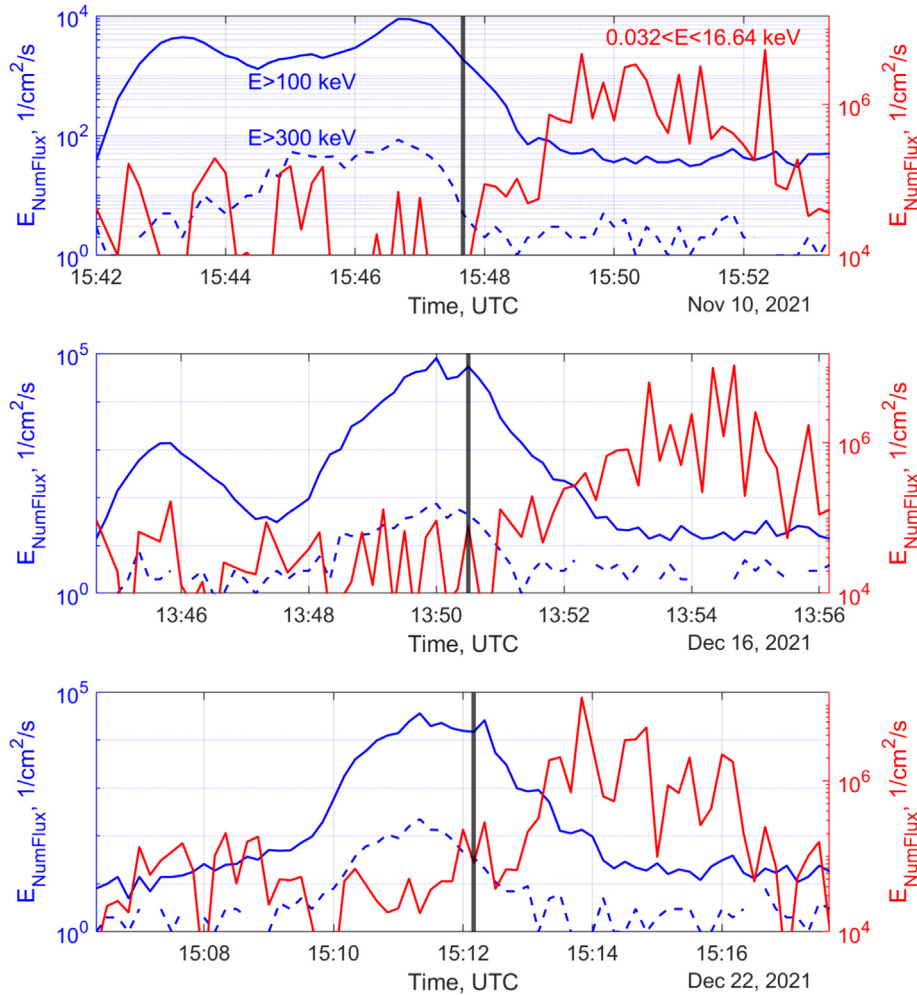


Fig. 5. METEOR-M2 charged particle measurements during three flights near VTL observatory. Blue lines demonstrate the high energy electrons fluxes: solid line – 100 keV, dashed line – 300 keV. Red line – low energy plasma flux (0.032–16.64 keV). Black vertical lines – the moments of UV-microbursts measurements.

Average sized microburst SAMPEX clusters last about 1 min, which coincides with the duration of a series of PAIPS flares (see right panel of Fig. 1 or examples in Fig. 7). Substantial microburst clusters in SAMPEX last several minutes. This time is determined by the size of the precipitation area and corresponds to the duration of SAMPEX flight through it. The process itself is much longer, thus, a direct comparison of satellite and ground-based detectors is complicated, because a satellite crosses a precipitation region for a couple of minutes while a ground-based detector remains in it for a long time, slowly shifting in longitude. The advantage of the second one is that it can study the temporal structure of the whole process of REM precipitation, but the satellite measures the spatial extension and provides a global picture due to “scanning” of the globe (15 orbits per day).

Indirect measurements of REM in the atmosphere previously were conducted using stratospheric balloons equipped with X-rays detectors (Anderson, & Milton, 1964; Lazutin and Roldugin, 1966; Lazutin and Charachcian, 1966). In this case the duration of measurements is limited by a balloon lifetime and can reach hours.

In (Siren et al., 1980) the analyses of simultaneous measurements of X-rays (25–500 keV) onboard the balloon launched above the vicinity of Roberval, Quebec (48.50° N, 72.25° W) on July 9, 1975 and the 30-MHz riometer located at the conjugate point (Siple, Antarctica, 75.94° S, 84.25° W) were made. The long X-ray groups (series of peaks) were measured which last for several minutes and consist of separate packets. It was shown that these X-ray microburst groups exhibit a one-to-one correspondence with time-delayed pulses of ionospheric absorption measured by a riometer which indicates an increase in the electron density at the altitude of the ionospheric D-region (60–90 km) (Little & Leinbach, 1959; Kero et al., 2014; Rogers & Honary, 2015). Additional ionization at these altitudes is determined by electron precipitation with energies higher than 30 keV. It was calculated that X-ray fluxes derived from exponential electron spectra (e-folding energies ranging from ~30 to 50 keV) always gave a close match to the data up to 250 keV. Interesting that for the 250 to 500 keV, the measured fluxes fell above the best fit exponential spectrum by a factor of 4 to 10. This is a consequence of the additional flux of more

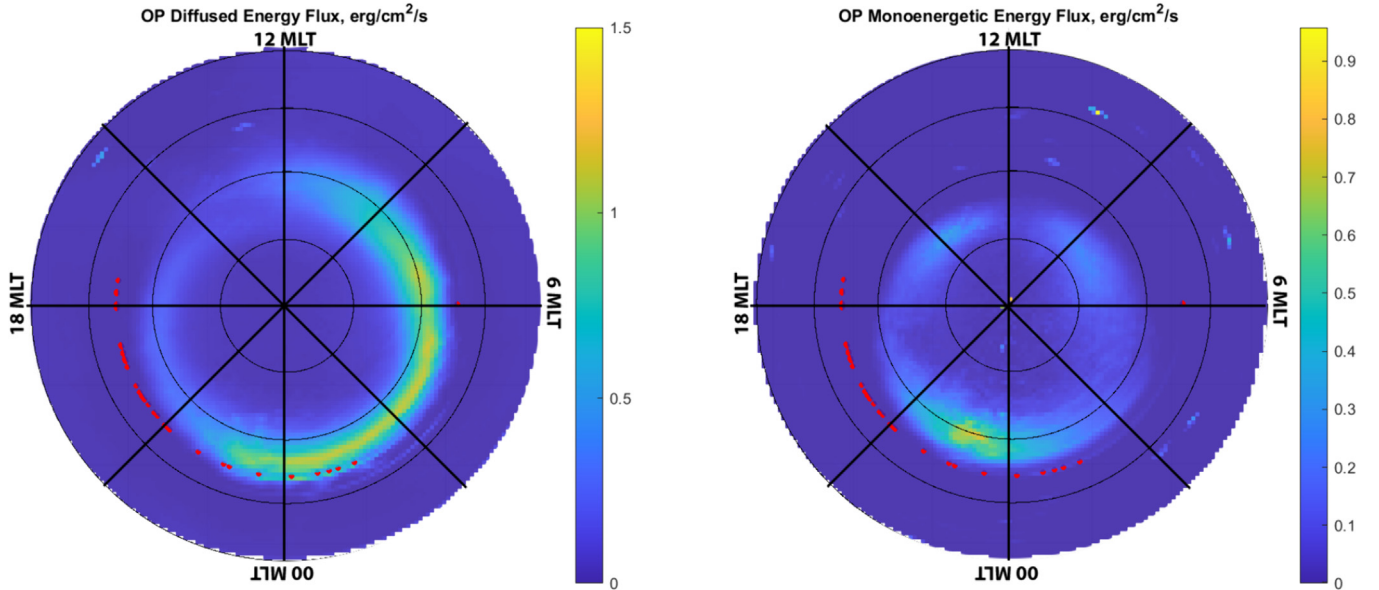


Fig. 6. UV-microbursts position (red dots) relative to the statistical distribution of the diffuse (left panel) and monoenergetic (right panel) electron precipitation in the auroral zone.

energetic electrons. The measured absorption in the conjugate point also exceeds the simulated values due to additional high-energy electrons as well as extra ionization of the D region by bremsstrahlung.

For one additional series of microbursts there was a possibility to compare with spectrometer data. These microbursts were found on March 2023 when a spectrometer was installed in addition to the main photometer. First of all, it demonstrated that microbursts are measured by two different techniques and the detectors artifact is eliminated. The distribution on FWHM of bursts is shown in Fig. 8. It is well seen that it confirms the distribution in Fig. 2. Moreover, it is similar for all three channels (391 and 337 of spectrometer and wide wavelength range of photometer). Number of measured bursts is different and it can be explained by the different sensitivity of the spectrometer and photometer since the diameter of the spectrometer's photomultiplier cathode is 1 cm while the entrance pupil diameter of the photometer is 5 cm.

The measurements in near-UV wavelength range and especially 337 nm may indicate relatively low altitude of the emission which is caused by high energy electrons (more than 100 keV) (Klimov et al., 2023).

If we look again to Figs. 4 and 5 it is interesting to note that similar measurements were done for UV pulsations on board the Lomonosov satellite (Klimov et al., 2022a). Namely, weak pulsations of UV intensity in the equatorial border of the aurora oval were observed simultaneously with the increased charged particles flux (with energies higher than 100 and 800 keV). The similar picture is observed in this study: UV-microbursts are placed lower in latitude than auroral oval and coincide with a position of high-energy precipitating electrons.

VTL observatory ($L_{VTL} = 6$) position is close to the maximum of REM L-shell distribution ($L \sim 5$). As one

can see from column 7 of Table A1 in Appendix A the UV-microbursts are measured in quite geomagnetic activity: the K_p index is lower than 3, mean value is 1^+ . The L distribution of the frequency of the REMs for various geomagnetic activity levels was studied based on data from the SAMPEX satellite and it was shown that maximum of distribution ($K_p < 3$) a peak occurrence at $L = 5.5$, while for $6.6 \leq K_p \leq 8.7$ a peak occurrence moves to $L = 4$.

Fig. 6 demonstrates that the majority of UV-microbursts are measured in the evening MLT sector, while REMs are mostly measured in the morning (Shumko et al., 2021). The occurrence frequency of relativistic microbursts has maximum at 8 MLT, it minimizes at 15 MLT (Douma et al., 2017). At the same time, there is a small population of relativistic microbursts occurring prior to midnight, from 20 to 24 MLT. The maximum of the REMs distribution over the MLT cannot be seen in the photometer data, because measurements are taken only in the dark. As well as the lack of events after midnight also may have a simple instrumental explanation. Aurora usually occurs after midnight and the atmosphere emission becomes much brighter, and short bursts of radiation become immeasurable, because the intensity of their radiation is significantly lower than the background. In addition, the response of the photometer to high radiation fluxes in the photon counting mode is not linear due to the pile-up effect. This leads to an additional decrease in the counting rate with short bright pulses against a large background. Thus a ground-based photometer measures primarily flashes at low background levels in the pre-midnight MLT sector.

The MLT of microbursts measurements may indicate different wave-particle interaction mechanisms responsible for measured effects. One open question concerning microburst is can they be caused by waves other than whistler

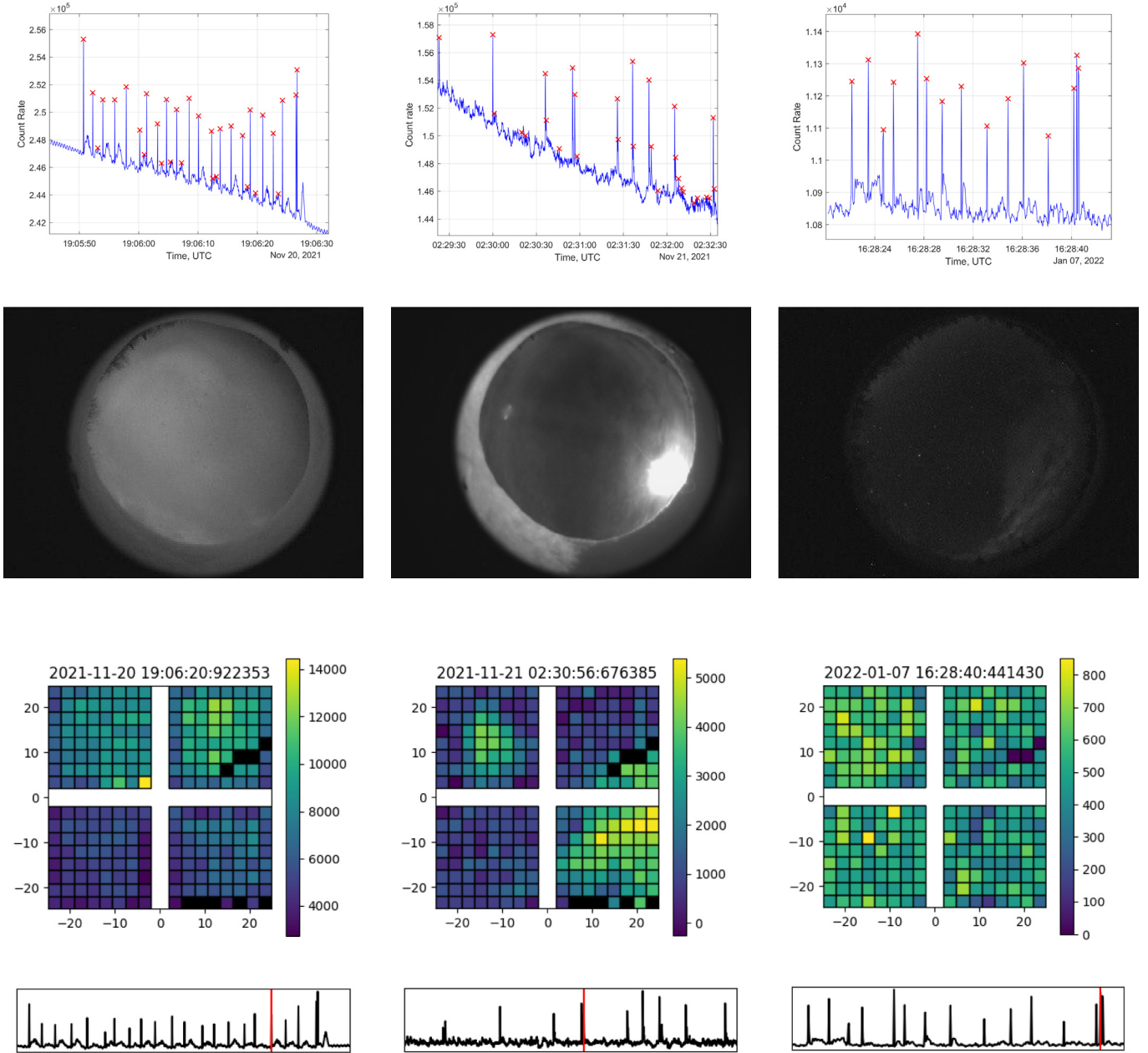


Fig. 7. Upper panel: UV-microbursts lightcurves for the events measured in different meteorological conditions (left: cloudy conditions, middle: thin transparent clouds, right: clear sky). Middle panel: ASC images. Bottom panel: photometer channel map for one peak and lightcurve with subtracted background; the corresponding peak is marked by red vertical line.

mode chorus waves, such as EMIC waves? It is widely accepted that microbursts are most often scattered by whistler mode chorus waves, and a number of simulations show that whistler mode chorus waves can rapidly scatter electrons over a wide range of energies. Douma et al. (2018) demonstrates by joint space and ground based observations that chorus waves are, most likely, the primary drivers of relativistic microbursts. But EMIC waves can also efficiently scatter electrons and protons and lead to microburst. In (Shumko et al., 2022) wave-particle interaction between EMIC waves, and magnetospheric protons and electrons is considered. And it is shown that this interaction resulted in a co-located isolated proton aurora and rel-

ativistic electron microbursts. Detailed analysis of the auroral emissions in (Shumko et al., 2022) suggests that no chorus waves were present during the event.

Chorus waves have been observed mainly on the morning side MLT (00–12 MLT) and across a wide range of L-shells. Nightside chorus is confined to $L \leq 8$, while strong dayside chorus can extend to higher L-shells (Li et al., 2009).

EMIC waves also have been observed across a wide range of L-shells and are most prevalent from 12 to 18 MLT during active conditions (Meredith et al., 2014). In addition it was shown that the occurrence of EMIC events is higher on the dayside than the nightside of the magneto-

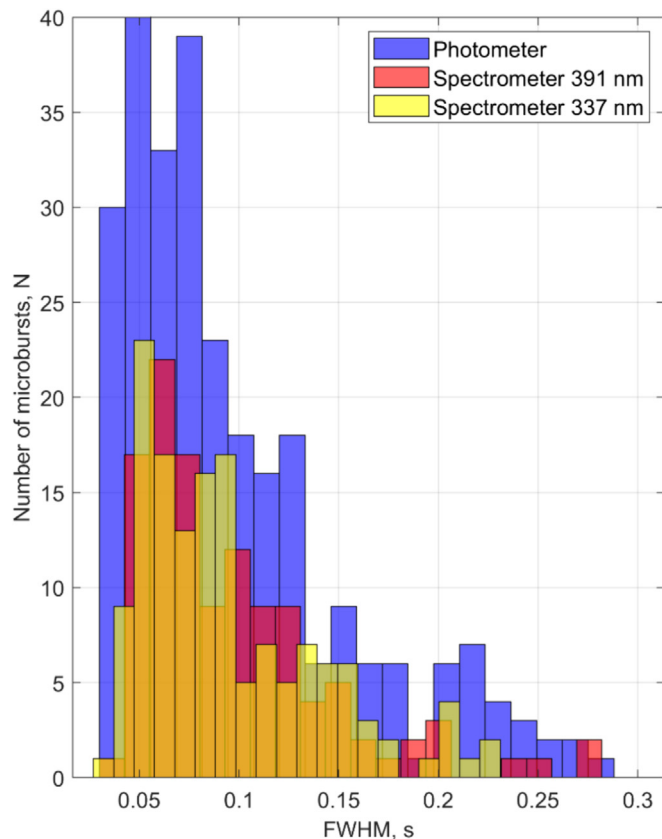


Fig. 8. UV-microburst measured simultaneously by photometer and spectrometer on March 2023 distribution on the FWHM.

sphere, for active periods (storms or substorms), the afternoon sector displays the highest occurrence rates (Saikin et al., 2016).

Thus, as mentioned above, the time of registration of events can be a marker indicating the type of electromagnetic waves responsible for the appearance of microbursts. In our case, if we accept the hypothesis that UV-microbursts are associated with precipitation of energetic particles, then the evening MLT sector is more likely to correspond to scattering by EMIC rather than by chorus waves.

5. Conclusions

The paper presents the results of the search and analysis of UV-microbursts in the data of the imaging photometer installed at the VTL in 2021. Data for the first season of work (2021/2022) was analyzed. 36 events with the following characteristics were detected:

- 1) Microbursts are measured in series with a duration from 10 s to ~ 1 h. Each pulse has a complicated structure with a single time sample (41 ms) high intensity peak and a subsequent prolonged afterglow.
- 2) Time interval between pulses is not constant and varies in a range between 100 ms and 5 s.

- 3) The typical amplitude is around 500–1000 counts, which approximately corresponds to the intensity of the emission on the entrance window of 10^4 – 10^5 photon/cm² sr s.

The probable source of UV-microbursts may be REMs, which are observed in satellite experiments at the same geomagnetic latitudes and have similar time characteristics. Satellite electron detectors as well as balloon-born X-ray measurements demonstrate that REM appear as clusters or series of sharp peaks. The same is observed in the PAIPS photometer.

UV-microbursts are mainly observed during low geomagnetic activity (average K_p index is 1+), in the evening sector of MLT. These observations are confirmed by earlier satellite data (SAMPEX), where it was found that REMs occur both during low geomagnetic activity, with the maximum frequency shifting towards $L = 6$, and in pre-midnight time (although the maximum frequency occurs at 8 MLT).

Observational conditions were classified into three characteristic cases: clouds, transparent clouds and clear sky. It was shown that the temporal structure of UV-microbursts does not depend on cloud presence. Spatial structure of the events may vary from event to event: from a uniform diffuse glow (both in the presence of clouds and without them) to individual local spots in the FOV of the photometer. All possible anthropogenic and instrumental origins of measured UV-microbursts are excluded.

UV-microbursts are not measured during active auroras and this can be explained by the peculiarities of the photometer's operation under high background conditions. Thus measured UV-microbursts are associated with precipitation of energetic particles scattered by EMIC rather than by chorus waves.

In February 2023, the photometer was supplemented with a spectrometer, and in October 2023, a second telescope was installed at the Lovozero Observatory, 150 km from VTL, which will allow stereometric measurements. Both of these additions will significantly increase the ability of the PAIPS system to study the temporal and vertical structure of the luminescence, which will provide answers regarding the nature of the observed UV-microbursts.

Data availability

The raw data that support the findings of this study are available from the corresponding author, (P.K.), upon reasonable request. Quick-looks and tables of events are available on the website of the PAIPS project (<https://uhcr.sinp.msu.ru/paips-en.html>).

Declaration of competing interest

The authors declare that they have no known competing financial interests or personal relationships that could have appeared to influence the work reported in this paper.

Acknowledgments

This research was funded by Russian Science Foundation grant number 22-62-00010 (<https://rscf.ru/project/22-62-00010/>).

We acknowledge use of NASA/GSFC's Space Physics Data Facility's OMNIWeb service, and OMNI data for IMF and SW data, K_p index (<https://omniweb.gsfc.nasa.gov/ow.html>, accessed on 07 January 2024). DMSP satellites data on particle precipitation were used for this study ([https://www.ncei.noaa.gov/data/dmsp-space-](https://www.ncei.noaa.gov/data/dmsp-space-weather-sensors/)

[weather-sensors/](https://www.ncei.noaa.gov/data/dmsp-space-weather-sensors/), accessed on 07 January 2024). METEOR-M2 satellite data on electron flux provided by the SINP MSU Space monitoring data center (<http://smdc.sinp.msu.ru/>, accessed on 07 January 2024). For aurora oval simulations a pure-python implementation of the Ovation Prime 2010 auroral precipitation model was used (<https://github.com/lkilcommons/OvationPyme>, accessed on 07 January 2024). The authors acknowledge the TUS and JEM-EUSO collaborations for the ability to use technologies developed in these collaborations for this study.

Appendix A Table A1 UV-microbursts event list.

N	Start Time, UTC	End Time, UTC	MLT, hours	Microbursts Average Amplitude, Counts	Observational conditions (cloud coverage)	K_p	IMF By, nT	IMF Bz, nT	SW Speed, km/s
1	13/10/21 18:13:55	13/10/21 18:14:31	20.96	71.6	clear sky	1 ⁻	3.22	-0.01	405.00
2	03/11/21 16:06:33	03/11/21 16:14:00	18.97–19.09	603.9	transparent clouds	1 ⁻	1.60	-0.51	501.70
3	10/11/21 15:18:45	10/11/21 15:21:20	18.26–18.30	95.5	transparent clouds	1 ⁻	2.81	1.47	429.70
4	10/11/21 15:37:18	10/11/21 15:50:30	18.55–18.74	99.9	transparent clouds	1 ⁻	0.64	1.64	423.60
5	13/11/21 16:51:45	13/11/21 16:53:00	19.65–19.68	217.0	no ASC data	0 ⁺	1.47	2.46	325.00
6	20/11/21 15:26:45	20/11/21 15:27:25	18.39	648.4	transparent clouds	3 ⁺	4.08	0.59	546.90
7	20/11/21 19:05:45	20/11/21 19:06:29	21.68	4181.4	clouds	2 ⁺	-0.36	3.52	532.50
8	21/11/21 2:29:00	21/11/21 2:32:35	5.15–5.2	2967.7	transparent clouds	3	-6.43	-1.29	622.00
9	21/11/21 15:30:36	21/11/21 15:31:14	18.45	300.1	clouds	3 ⁺	-0.03	2.44	634.70
10	23/11/21 16:25:40	23/11/21 16:27:41	19.25–19.28	189.5	transparent clouds	3 ⁻	-1.72	-1.65	510.40
11	27/11/21 22:06:44	27/11/21 22:16:41	0.53–0.7	155.4	clear sky	3	-2.25	3.06	298.00
12	29/11/21 14:13:30	29/11/21 15:57:42	17.25–18.83	646.5	14:13–14:50 – transparent clouds; 14:50–15:57 – clouds	1 ⁻	-4.02	-1.80	349.00
13	11/12/21 14:15:38	11/12/21 14:32:00	17.23–17.50	336.7	clouds	0	no data	no data	no data
14	12/12/21 15:14:17	12/12/21 15:52:46	18.14–18.69	1026.5	clouds	1	-3.41	-3.03	295.10
15	16/12/21 13:44:13	16/12/21 13:53:09	16.69–16.84	1011.4	clouds	1	-1.12	4.87	529.90
16	16/12/21 14:00:52	16/12/21 14:01:46	16.96	836.5	clouds	1	-1.47	4.69	528.00
17	16/12/21 14:02:40	16/12/21 14:16:33	16.99–17.22	966.7	clouds	1	-1.61	4.69	528.20
18	22/12/21 14:02:24	22/12/21 14:42:34	16.94–17.58	433.6	clouds	3	-1.69	-0.90	593.00
19	22/12/21 14:42:34	22/12/21 16:01:58	17.58–18.75	525.3	clouds	2	-2.75	1.66	602.00
20	22/12/21 16:01:58	22/12/21 17:03:00	18.75–19.62	791.4	clouds	2	-2.22	-0.61	573.60
21	25/12/21 20:50:42	25/12/21 20:51:08	23.06	652.6	clouds	2 ⁻	-1.14	-1.93	424.40
22	25/12/21 21:57:06	25/12/21 22:01:44	0.14–0.21	487.3	clouds	1 ⁻	-1.81	-2.62	425.00
23	06/01/22 14:33:33	06/01/22 14:33:54	17.31	1511.5	clouds	0	2.26	1.70	348.00
24	06/01/22 15:28:36	06/01/22 15:31:26	18.16–18.2	1084.0	clouds	0	1.23	2.80	351.6
25	06/01/22 17:00:08	06/01/22 17:10:25	19.48–19.60	1061.9	clouds	0	4.63	-0.07	347.10
26	06/01/22 17:37:46	06/01/22 17:38:01	20	993.6	clouds	0	4.44	0.01	352.00
27	06/01/22 20:09:35	06/01/22 20:11:54	22.33–22.37	1179.2	clouds	0 ⁺	2.61	0.43	347.20
28	07/01/22 15:37:35	07/01/22 15:40:48	18.28–18.33	2364.5	clouds	0	2.37	1.15	308.50
29	07/01/22 16:28:20	07/01/22 16:28:43	19.01	412.7	clear sky	0	1.96	1.44	311.30
30	07/01/22 17:47:53	07/01/22 17:48:28	20.14	195.1	clear sky	0	1.74	1.91	310.90
31	07/01/22 21:49:00	07/01/22 21:50:35	23.93–23.95	137.9	clear sky	0	1.54	0.23	299.10
32	08/01/22 16:52:31	08/01/22 16:53:22	19.35	1707.6	clouds	1 ⁺	5.12	-2.20	307.00
33	09/01/22 17:22:00	09/01/22 17:23:00	19.77–19.78	363.5	clear sky	1 ⁺	0.06	0.46	441.40
34	09/01/22 17:43:25	09/01/22 17:46:55	20.07–20.11	339.1	transparent clouds	1 ⁺	-0.46	-0.01	442.20
35	29/01/22 21:36:55	29/01/22 21:37:30	23.70	1203.2	transparent clouds	1	4.06	1.20	505.00
36	05/02/22 19:22:54	05/02/22 19:38:55	21.55–21.80	1513.3	transparent clouds	3 ⁻	-3.26	3.10	573.20

Column 1 – Number of the event. Columns 2, 3 – time interval of the event (UTC). Column 3 – MLT interval of the event (mean value for events shorter than 1 min). Column 4 – Average amplitude of pulses. Column 5 – Observations conditions during the event based on ASC data (clouds, transparent clouds or clear sky). Column 6 – Geomagnetic activity during the event (K_p index). Column 7, 8 – Data used for aurora oval simulations with OVATION-Prime: two components of interplanetary magnetic field (By and Bz) and Solar wind speed.

References

- Abraham, J., Abreu, P., Aglietta, M., et al., 2010. The fluorescence detector of the Pierre Auger Observatory. *Nucl. Instrum. Methods Phys. Res.* 620 (2–3), 227–251. <https://doi.org/10.1016/j.nima.2010.04.023>.
- Anderson, K., Milton, D., 1964. Balloon observations of X rays in the auroral zone: 3. High time resolution studies. *J. Geophys. Res.* 69 (21), 4457–4479. <https://doi.org/10.1029/JZ069i021p04457>.
- Belov, A., Klimov, P., Kozelov, B., et al., 2022. Optical complex for the study of pulsating aurora with sub-millisecond time resolution on the basis of the Verkhnetulomsky observatory. *J. Atmos. Sol.-Terr. Phys.* 105905 <https://doi.org/10.1016/j.jastp.2022.105905>.
- Blake, J., Looper, M., Baker, D., et al., 1996. New high temporal and spatial resolution measurements by SAMPEX of the precipitation of relativistic electrons. *Adv. Space Res.* 18, 171–186. [https://doi.org/10.1016/0273-1177\(95\)00969-8](https://doi.org/10.1016/0273-1177(95)00969-8).
- Casolino, M., Barghini, D., Battisti, M., et al., 2023. Observation of nighttime emissions of the Earth in the near UV range from the International Space Station with the Mini-EUSO detector. *Remote Sens. Environ.* 284113336. <https://doi.org/10.1016/j.rse.2021.113336>.
- Claudepierre, S.G., Ma, Q., Bortnik, J., et al., 2020. Empirically estimated electron lifetimes in the Earth's radiation belts: Comparison with theory. *Geophys. Res. Lett.* 47 (3), e2019GL086056. <https://doi.org/10.1029/2019GL086056>.
- Douma, E., Rodger, C.J., Blum, L., et al., 2017. Occurrence characteristics of relativistic electron microbursts from SAMPEX observations. *J. Geophys. Res.* 122 (8), 8096–8107. <https://doi.org/10.1002/2017JA024067>.
- Douma, E., Rodger, C.J., Clilverd, M.A., et al., 2018. Comparison of relativistic microburst activity seen by SAMPEX with ground-based wave measurements at Halley. *Antarctica. J. Geophys. Res.* 123, 1279–1294. <https://doi.org/10.1002/2017JA024754>.
- Douma, E., 2018. Relativistic Electron Microbursts: Properties and Possible Plasma Wave Drivers (Doctoral dissertation). University of Otago.
- Greeley, A., Kanekal, S., Baker, D., et al., 2019. Quantifying the contribution of microbursts to global electron loss in the radiation belts. *J. Geophys. Res.* 124 (2), 1111–1124. <https://doi.org/10.1029/2018JA026368>.
- Hall, R.C., 2001. A history of the military polar orbiting meteorological satellite program. Office of the Historian, National Reconnaissance Office. [Available at <https://www.nro.gov/history/csnr/programs/docs/prog-hist-02.pdf>].
- Jaynes, A., Lessard, M., Takahashi, K., et al., 2015. Correlated Pc4-5 ULF waves whistler-mode chorus and pulsating aurora observed by the Van Allen Probes and ground-based systems. *J. Geophys. Res.* 120. <https://doi.org/10.1002/2015JA021380>.
- Kataoka, R., Fukuda, Y., Uchida, H., et al., 2016. High-speed stereoscopy of aurora. *Ann. Geophys.* 34, 41–44. <https://doi.org/10.5194/angeo-34-41-2016>.
- Kero, A., Vierinen, J., McKay-Bukowski, D., et al., 2014. Ionospheric electron density profiles inverted from a spectral riometer measurement. *Geophys. Res. Lett.* 41. <https://doi.org/10.1002/2014GL060986>.
- Klimov, P., Panasyuk, M., Khrenov, B., et al., 2017. The TUS detector of extreme energy cosmic rays on board the Lomonosov satellite. *Space Sci. Rev.* 212. <https://doi.org/10.1007/s11214-017-0403-3>.
- Klimov, P., Khrenov, B., Kaznacheeva, M., et al., 2019. Remote sensing of the atmosphere by the ultraviolet detector TUS onboard the Lomonosov satellite. *Remote Sens. (Basel)* 11, 2449. <https://doi.org/10.3390/rs11202449>.
- Klimov, P., Kalegaev, V., Sigaeva, K., et al., 2022a. Near-UV pulsations in the aurora region measured by orbital telescope TUS during high-intensity and long-duration continuous AE activity. *Remote Sens. (Basel)* 15, 147. <https://doi.org/10.3390/rs15010147>.
- Klimov, P., Sharakin, S., Belov, A., et al., 2022b. System of imaging photometers for upper atmospheric phenomena study in the arctic region. *Atmosphere* 13, 1572. <https://doi.org/10.3390/atmos13101572>.
- Klimov, P., Nikolaeva, V., Belov, A., et al., 2023. Variations in pulsating aurora emission in 337 nm and 391 nm nitrogen spectral lines during geomagnetic substorms. *Universe* 9, 441. <https://doi.org/10.3390/universe9100441>.
- Kozelov, B., Pilgaev, S., Borovkov, L.P., et al., 2011. Multi-scale auroral observations in Apatity: Winter 2010–2011. *Geosci. Instrum. Methods Data Syst. Discuss.* 1. <https://doi.org/10.5194/gid-1-31-2011>.
- Kugusheva, A., Kalegaev, V., Vlasova, N., et al., 2021. Space-time structure of energetic electron precipitations according to the data of balloon observations and polar satellite measurements on February 1–6 2015. *Cosm. Res.* 59, 446–455. <https://doi.org/10.1134/S0010952521060058>.
- Lazutin, L., Charachian, T., 1966. On the spatial and temporal features of the electron precipitating into the auroral zone stratosphere by balloon and riometers measurements. *Izvestiya Academ. Nauk, phys. serie*, 30, N 11. (in Russian).
- Lazutin, L., Roldugin, V., 1966 X-ray bursts and polar aurora. *Izvestiya Academ. Nauk, phys. serie*, 30, N 11. (in Russian).
- Li, W., Thorne, R., Angelopoulos, V., et al., 2009. Global distribution of whistler-mode chorus waves observed on the THEMIS spacecraft. *Geophys. Res. Lett.* 36, L09104. <https://doi.org/10.1029/2009GL013759>.
- Little, C., Leinbach, H., 1959. The riometer—a device for the continuous measurement of ionospheric absorption. *Proc. IRE* 47 (2), 315–320. <https://doi.org/10.1002/2014GL060986>.
- Lorentzen, K., Blake, J., Ina, U., et al., 2001. Observations of relativistic electron microbursts in association with VLF chorus. *J. Geophys. Res.* 106, 6017–6027. <https://doi.org/10.1029/2000ja003018>.
- Marshall, R., Da Silva, C., Pasko, V., 2015. Elve doublets and compact intracloud discharges. *Geophys. Res. Lett.* 42 (14), 6112–6119. <https://doi.org/10.1002/2015GL064862>.
- Meredith, N., Horne, R., Kersten, T., et al., 2014. Global morphology and spectral properties of EMIC waves derived from CRRES observations. *J. Geophys. Res.* 119 (7), 5328–5342. <https://doi.org/10.1002/2014JA020064>.
- Miyoshi, Y., Oyama, S., Saito, S., et al., 2015. Energetic electron precipitation associated with pulsating aurora: EISCAT and Van Allen Probe observations. *J. Geophys. Res. (Space Phys.)* 120 (4), 2754–2766. <https://doi.org/10.1002/2014JA020690>.
- Miyoshi, Y., Saito, S., Kurita, S., et al., 2020. Relativistic electron microbursts as high-energy tail of pulsating aurora electrons. *Geophys. Res. Lett.* 47. <https://doi.org/10.1029/2020GL090360>.
- Newell, P., Sotirelis, T., Liou, K., et al., 2007. A nearly universal solar wind-magnetosphere coupling function inferred from 10 magnetospheric state variables. *J. Geophys. Res.* 112 (A1). <https://doi.org/10.1029/2006JA012015>.
- Newell, P., Sotirelis, T., Wing, S., 2009. Diffuse, monoenergetic, and broadband aurora: the global precipitation budget. *J. Geophys. Res.* 114 (A9). <https://doi.org/10.1029/2009JA014326>.
- Newell, P., Sotirelis, T., Wing, S., 2010. Seasonal variations in diffuse, monoenergetic, and broadband aurora. *J. Geophys. Res.* 115 (A3). <https://doi.org/10.1029/2009ja014805>.
- Nishimura, Y., Lessard, M., Katoh, Y., et al., 2020. Diffuse and Pulsating Aurora. *Sp. Sci. Rev.* 216. <https://doi.org/10.1007/s11214-019-0629-3>.
- O'Brien, T., Lorentzen, K., Mann, I., et al., 2003. Energization of relativistic electron in the response of ULF power and MeV microbursts: Evidence for dual ULF and VLF acceleration. *J. Geophys. Res.* 108, 1329. <https://doi.org/10.1029/2002ja009784>.
- Redmon, R., Denig, W., Kilcommons, L., et al., 2017. New DMSP database of precipitating auroral electrons and ions. *J. Geophys. Res.* 122 (8), 9056–9067. <https://doi.org/10.1002/2016JA023339>.

- Rogers, N.C., Honary, F., 2015. Assimilation of real-time riometer measurements into models of 30 MHz polar cap absorption. *J. Space Weather Space Clim.* 5, A8. <https://doi.org/10.1051/swsc/2015009>.
- Saikin, A., Zhang, J., Smith, C., et al., 2016. The dependence on geomagnetic conditions and solar wind dynamic pressure of the spatial distributions of EMIC waves observed by the Van Allen Probes. *J. Geophys. Res.* 121 (5), 4362–4377. <https://doi.org/10.1002/2016JA022523>.
- Shumko, M., Blum, L., Crew, A., 2021. Duration of individual relativistic electron microbursts: a probe into their scattering mechanism. *Geophys. Res. Lett.* 48e2021GL093879. <https://doi.org/10.1029/2021GL093879>.
- Shumko, M., Gallardo-Lacourt, B., Halford, A., et al., 2022. Proton aurora and relativistic electron microbursts scattered by electromagnetic ion cyclotron waves. *Front. Astron. Space Sci.* 9975123. <https://doi.org/10.3389/fspas.2022.975123>.
- Siren, J., Rosenberg, T., Detrick, D., et al., 1980. Conjugate observation of electron microburst groups by Bremsstrahlung X ray and riometer techniques. *J. Geophys. Res.* 85 (A12), 6760. <https://doi.org/10.1029/ja085ia12p06760>.
- Tesema, F., Partamies, N., Nesse, T.H., et al., 2020. Observations of precipitation energies during different types of pulsating aurora. *Ann. Geophys.* 38 (6), 1191–1202. <https://doi.org/10.5194/angeo-38-1191-2020>.
- Tokuno, H., Tameda, Y., Takeda, M., et al., 2011. New air fluorescence detectors employed in the Telescope Array experiment. *Nucl. Instrum. Methods Phys. Res.* 676. <https://doi.org/10.1016/j.nima.2012.02.044>.
- Turunen, E., Verronen, P., Seppälä, A., et al., 2009. Impact of different energies of precipitating particles on NO_x generation in the middle and upper atmosphere during geomagnetic storms. *J. Atmos. Sol.-Terr. Phys.* 71, 1176–1189. <https://doi.org/10.1016/j.jastp.2008.07.005>.